Amorphous TiO_2 from a statistical view based on molecular dynamics using machine learning interatomic potentials

Xuwei Gong,[1,2,*] Lingyan Lu,[1,2,*] Jun Chai,[3,†] Chi Song,[1,‡] Chen Ming,[1,2] and Yi-Yang Sun[1,2]

[1] *State Key Laboratory of High-Performance Ceramics, Shanghai Institute of Ceramics, Chinese Academy of Sciences, Shanghai 201899, China*

[2] *Center of Materials Science and Optoelectronics Engineering, University of Chinese Academy of Sciences, Beijing 100049, China*

[3] *College of Chemical and Material Engineering, Quzhou University, Quzhou, Zhejiang 324000, China*

We use molecular dynamics with a machine-learning interatomic potential based on the higher-order equivariant message-passing atomic cluster expansion (MACE) framework to construct an ensemble of 100 amorphous TiO_2 configurations. The final structures are subject to variable-cell relaxations using density functional theory calculations, where PBEsol functional is adopted as it reproduces the experimental densities for all the three crystalline phases, namely, rutile, anatase and brookite. The mean density is calculated to be 3.94 $\mathrm{g\,cm^{-3}}$. While the ensemble is dominated by 6-coordinated Ti and 3-coordinated O, the corresponding percentage is 57.4% and 66.8% only. There exist 28.9% of 5-coordinated Ti, 12.1% 7-coordinated Ti, 21.4% 2-coordinated 21.4% O and 11.8% 4-coordinated O. Using hybrid HSE06 functional with the exact-exchange fraction (α) set to 0.18, the ensemble average yields a band gap of 3.44 ± 0.12 eV for the amorphous phase, which is greater than those of the three crystalline phases obtained using the same computational framework, namely, variable-cell relaxation using PBEsol and band gap calculation using HSE06 (α=0.18). Analysis of the density of states suggests that the band-gap widening in the amorphous phase is associated with the narrowed Ti 3*d* band. It is potentially useful to adopt the protocol in this work to study the effect of amorphization on the electronic structures of other semiconductors.

Keywords: amorphous, TiO_2, molecular dynamics, machine-learning interatomic potential, band gap

PACS: 61.43.Dq, 02.70.Ns, 07.05.Mh, 71.23.Cq

I. INTRODUCTION

Titanium dioxide (TiO_2) is a prototypical wide-band-gap transition-metal oxide with applications in photocatalysis, photoelectrochemistry, optical coatings, solar-energy conversion, and electronic devices.[1–6] In addition to the well-known rutile, anatase, and brookite polymorphs, amorphous TiO_2 (a-TiO_2) is technologically important. It can be deposited at relatively low temperatures as uniform and conformal thin films.[5, 7] Such films have been used as protective layers that suppress photocorrosion while permitting charge transport at semiconductor–electrolyte interfaces.[5, 8] Their performance is governed not only by chemical composition and defect concentration, but also by the intrinsic electronic structure of the disordered Ti–O network.[8–11] These capabilities establish a-TiO_2 as a functional material and motivate a detailed understanding of its structure-property relationships.

The loss of long-range periodicity in a-TiO_2 does not imply a complete loss of local structural order. Diffraction measurements and atomistic simulations show that the amorphous network retains short-range Ti–O coordination while exhibiting broad distributions of coordination numbers, Ti–O bond lengths, bond angles, and connections between neighboring TiO_x polyhedra.[7, 12–17] These structural variations directly influence the Ti–O orbital interactions that determine the band edges. Despite extensive study, even the direction of the band-gap change upon amorphization remains unsettled.[7, 15–22] For example, Landmann *et al.* reported an amorphous electronic gap obtained by HSE06 larger than those of rutile and brookite but close to that of anatase, together with quasiparticle and optical gaps of approximately 3.7 and 3.5 eV, respectively.[18] In contrast, Meng *et al.* yielded an HSE06 gap of 2.74 eV, smaller than the calculated gaps of the crystalline polymorphs.[7] Direct comparison among these results is complicated by differences in structural models, density, system size, quench protocol, exchange–correlation treatment, and the definition of the reported gap, which may refer to a Kohn–Sham, fundamental, optical, or mobility gap.

Constructing a statistically meaningful ensemble at first-principles accuracy remains a computational challenge. Melt–quench ab initio molecular dynamics (AIMD) provides a direct route to disordered structures, but its computational cost restricts accessible system sizes, trajectory lengths, and quench rates. Consequently, most previous electronic-structure studies have considered only one or a few models.[7, 15–18] A notable exception is the work of Mora-Fonz *et al.*,[20] who investigated the trapping of excess electrons and holes in bulk a-TiO_2 using hybrid density-functional theory. Their analysis was based on an ensemble of 50 amorphous struc-

* These authors contributed equally to this work.

† chaijun@qzc.edu.cn

‡ songchi21@mails.ucas.ac.cn

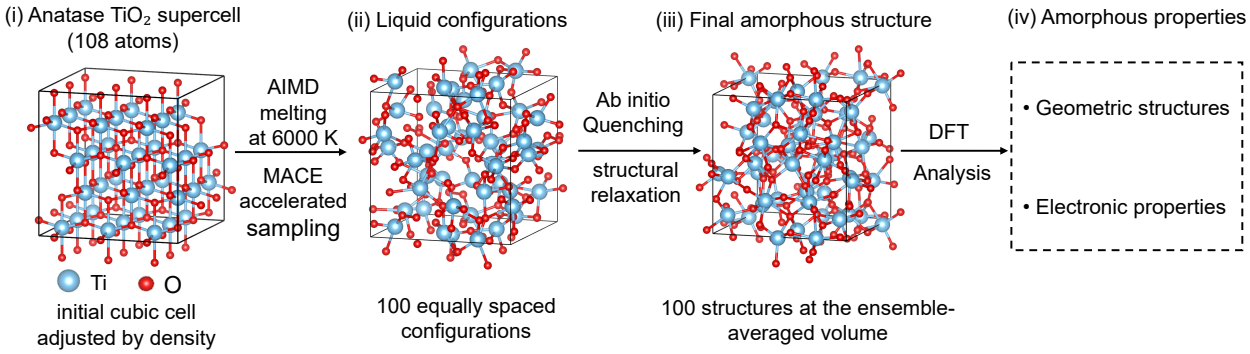


FIG. 1. Computational workflow for the generation and characterization of amorphous TiO_2 models.

tures, for which they reported an average gap of 3.25 eV. Machine-learning interatomic potentials offer a practical route to substantially broader structural sampling while retaining accuracy derived from first-principles reference data. Deep neural-network potentials have already enabled large-scale simulations of liquid and amorphous TiO_2, including systematic examinations of system size, cooling rate, pressure, and interfaces.[23–26]

In this work, we combine DFT-based AIMD with the higher-order equivariant message-passing atomic cluster expansion (MACE) framework[27] to establish an ensemble-based description of a-TiO_2. The MACE model is trained on the energies and forces of equilibrated high-temperature AIMD configurations and is then used to extend the sampling of the liquid state prior to quenching and zero-temperature relaxation. The resulting amorphous structures are characterized using radial and angular distribution functions, coordination statistics, and TiO_n polyhedral connectivity. Their electronic structures are subsequently evaluated at the hybrid-functional level. Comparing the gap distributions and the corresponding densities of states, we find that amorphization on average widens the gap. These results separate the systematic electronic consequences of amorphization from configuration-to-configuration fluctuations and demonstrate the importance of statistical structural sampling for describing the electronic structure of amorphous phase.

II. COMPUTATIONAL METHODS

All first-principles calculations in this work were performed using the DS-PAW package.[28] The interactions between the ionic cores and valence electrons were described using the projector-augmented-wave method,[29, 30] and the electronic wave functions were expanded in a plane-wave basis set. The computational procedure consisted of three stages: generation of an ensemble of amorphous TiO_2 structures using a combination of AIMD and machine-learning interatomic potential, statistical characterization of their structures, and calculation of their electronic properties. The overall computational workflow is summarized in Fig. 1.

Amorphous TiO_2 (a-TiO_2) models were generated using a melt–quench molecular-dynamics protocol. The initial configuration was constructed by a $3 \times 3 \times 1$ repetition of the conventional tetragonal anatase unit cell, which contains four TiO_2 formula units. The resulting periodic supercell contained 108 atoms, comprising 36 Ti and 72 O atoms. The initial tetragonal supercell, with a mass density of $3.89\,\mathrm{g\,cm^{-3}}$, was transformed into a cubic simulation box while preserving the density. The change in cell geometry distorted the Ti–O bond lengths and bond angles, providing an initial configuration for the subsequent melting simulation.

The AIMD simulation was performed using DS-PAW with the PBEsol exchange–correlation functional,[31] a plane-wave cutoff energy of 285 eV, Γ-point sampling, and an electronic self-consistency threshold of 10^{-5} eV. The distorted initial structure was melted at 6000 K in the canonical (NVT) ensemble using a Nosé–Hoover thermostat.[32, 33] The elevated temperature was selected to achieve high atomic diffusivity in the liquid state (albeit under high pressure due to the constraint on supercell size) for accelerated sampling of the configurational space within our accessible simulation time. This choice was partly guided by our previous melt-quench study of silica glass, where 6000 K was sufficient to yield relatively linear mean-squared displacement (MSD).[34] The simulation was propagated for 25,000 steps with a time step of 1 fs. After the first 5000 configurations were discarded to remove the memory of the initial crystalline configuration, 20,000 subsequent configurations and their total energies and atomic forces were retained. The configurations were randomly shuffled and divided into training, validation, and test sets containing 16,000, 2,000, and 2,000 configurations, respectively. A system-specific machine-learning interatomic potential was trained using the MACE framework.[27] Both the DFT total energies and force components were included as training targets. Specifically, the MACE potential employed a cutoff radius of 6.0 Å and two message-passing interaction layers, each with a correlation order of 3. The model used 128

message-passing channels with hidden irreducible representations of $128 \times 0e + 128 \times 1o$. The energy and force terms in the loss function were assigned weights of 1 and 100, respectively. Model optimization was performed for 300 epochs using the Adam optimizer with AMSGrad enabled. The initial learning rate was 0.001 and was reduced by a factor of 0.8 when the validation loss did not improve for 50 consecutive epochs. The trained MACE potential was interfaced with the Atomic Simulation Environment (ASE)[35] and used to extend the liquid-state trajectory at 6000 K in the NVT ensemble. The MACE-driven molecular-dynamics simulation was performed for 100,000 steps with a time step of 0.1 fs. One hundred liquid configurations were extracted from the trajectory at equal time intervals.

Each liquid configuration was then quenched independently to 0 K at a cooling rate of 1000 $\mathrm{K\,ps^{-1}}$ with a 1 fs time step. The resulting structures were relaxed with respect to both cell parameters and ionic positions (400 eV plane-wave cutoff) until the maximum residual force fell below 0.025 $\mathrm{eV\,\AA^{-1}}$. To remove volume difference across the ensemble, all 100 structures were then mapped onto a common cubic cell whose edge length was the cube root of the mean relaxed volume, and the internal coordinates were re-optimized at fixed cell shape and volume. The ensemble therefore shares a single composition, volume, and mass density, so that structural and electronic properties can be compared on a statistical basis. Electronic structure was evaluated for every member of the ensemble with the HSE06 functional, [36, 37] using an exact-exchange fraction $\alpha = 0.18$ and Γ-point sampling. The band gap and density of states were extracted for each configuration.

III. RESULTS AND DISCUSSION

A. Band structures of the crystalline polymorphs

Before examining the effects of amorphization on the electronic structure of TiO_2, it is necessary to establish a reference for the crystalline polymorphs. Band structures for rutile, anatase, and brookite were therefore computed using the HSE06 functional (Fig. 2). The rutile and brookite gaps of 2.92 and 3.37 eV are both direct at Γ point. For anatase, an indirect gap of 3.19 eV is obtained between the conduction band minimum at Γ and the valence band maximum along the Σ path, at 0.89 of the way from Γ to M, smaller than the direct Γ-point gap of 3.31 eV. Both band-edge locations agree with those reported by Landmann *et al.* [21]. The absolute values differ because the exact-exchange fraction adopted here is smaller than the standard HSE06 value of 0.25. The value of α was calibrated against the experimental anatase gap 3.20 eV. Unlike a periodic crystal, a-TiO_2 does not possess a unique representative unit cell, and the gap obtained from a single configuration can be affected by local coordination environments. Having established the crystalline baseline, we next evaluate the accuracy of the MACE potential used to generate the amorphous structural ensemble.

B. MACE model

The predictive accuracy of the trained MACE model was assessed on a held-out test set excluded from model optimization. Figure 3 compares the MACE predictions against the reference values for total energies and force components. The corresponding error metrics are given in the figure. The energy RMSE is 9.48 meV/atom and the force RMSE is 0.38 eV/Å. These errors are larger than those typically reported for machine-learned potentials. This is primarily a consequence of the 6000 K sampling temperature. The elevated errors also reflect the limited size of the present training set, which was drawn from a single AIMD trajectory; extending that trajectory would provide broader coverage of configuration space and is expected to reduce both metrics systematically. The potential is used solely to generate an ensemble of amorphous topologies through melt–quench cycles, and every resulting configuration is subsequently relaxed at the DFT level. Because the quantity of interest is the statistical distribution of band gaps across the ensemble rather than the energy or forces of any individual configuration, the present level of accuracy is adequate.

C. Atomic structure of a-TiO_2

Figure 4 shows the distribution of calculated densities for the 100 fully optimized a-TiO_2 configurations. The densities range from 3.78 to 4.10 $\mathrm{g\,cm^{-3}}$, with an ensemble mean of $\bar{\rho} = 3.94\ \mathrm{g\,cm^{-3}}$. This value lies between the PBEsol densities of anatase (3.89 $\mathrm{g\,cm^{-3}}$) and those of brookite and rutile (4.14 and 4.27 $\mathrm{g\,cm^{-3}}$). These calculated crystalline densities agree within 0.5% with the corresponding experimental values of 3.89, 4.13, and 4.25 $\mathrm{g\,cm^{-3}}$,[38, 39], respectively. The mean density of the amorphous ensemble falls within the experimental range of approximately 3.5–4.1 $\mathrm{g\,cm^{-3}}$ reported for a-TiO_2 films,[23] while previous calculations yielded 3.68[14] and 4.18 $\mathrm{g\,cm^{-3}}$.[40]

The local structure of a-TiO_2 was characterized through the partial radial distribution functions (RDFs) for the Ti–O, O–O, and Ti–Ti pairs. Figure 5 shows the RDFs averaged over the 100 final configurations. The Ti–O RDF exhibits a pronounced first maximum at 1.93 Å, demonstrating that the amorphous network retains a first Ti–O coordination shell. This position agrees well with the Ti–O maxima of 1.91–1.95 Å reported for previous melt–quenched models and with experimental first-neighbor distances of approximately 1.89–1.96 Å.[7, 12, 16]

The first O–O maximum is located at 2.72 Å, close to the experimental value of 2.67 Å and the calcu-

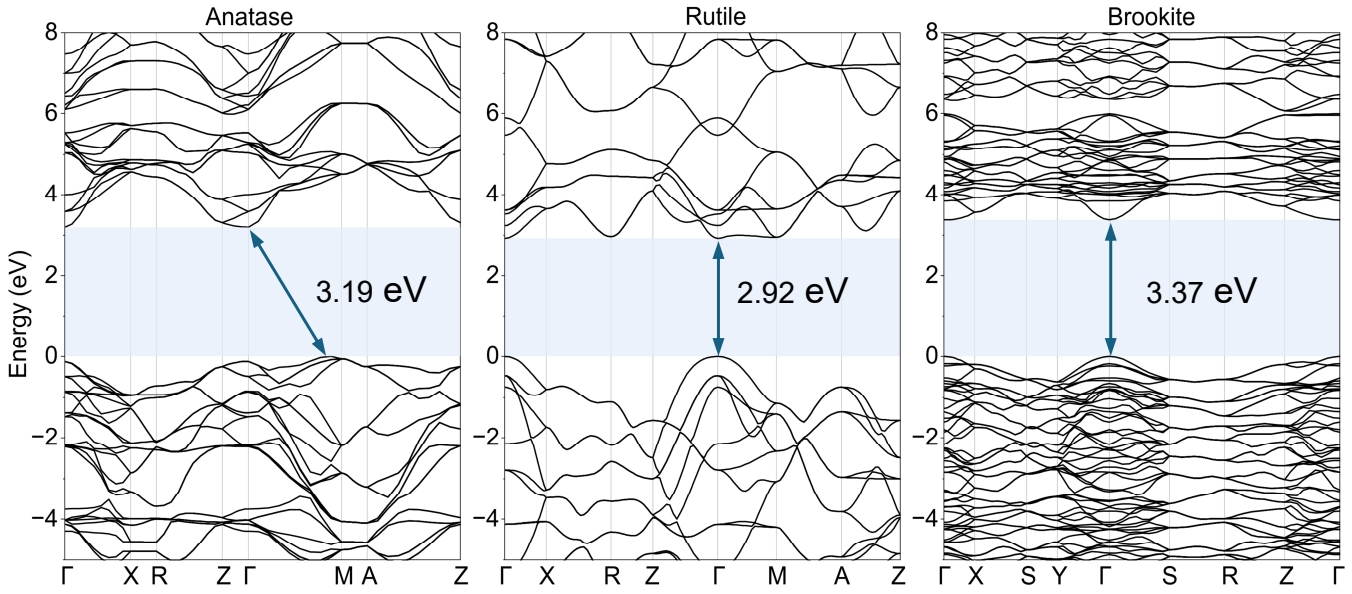


FIG. 2. Band structures of anatase, rutile, and brookite TiO_2, calculated with the HSE06 functional using an exact-exchange parameter $\alpha = 0.18$. Energies are referenced to the valence-band maximum of each polymorph.

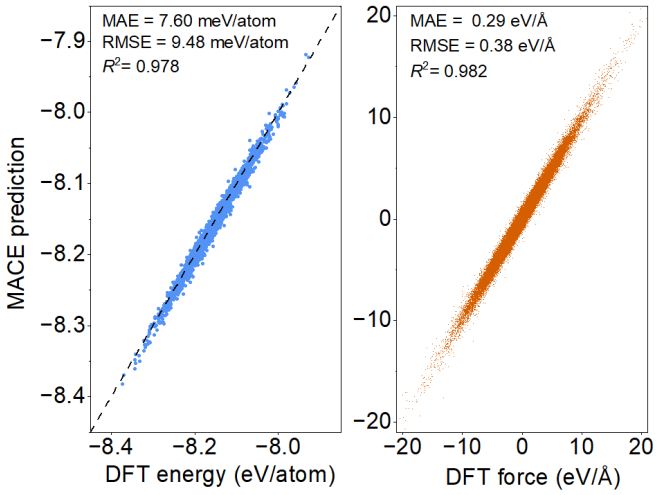


FIG. 3. Parity plots comparing the MACE predictions with the DFT reference values for the test set. Left panel shows the comparison for the total energies and right panel for the forces. The corresponding mean absolute error (MAE), root-mean-square error (RMSE), and coefficient of determination (R^2) are given in each panel.

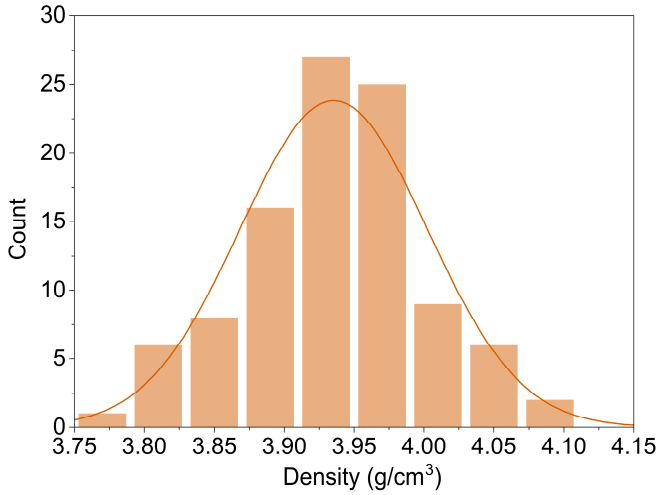


FIG. 4. Distribution of the calculated density for the 100 *a*-TiO_2 structures obtained by variable-cell relaxations using the PBEsol functional. The mean density is 3.94 g cm^{-3}. A bin width of 0.04 g cm^{-3} was used. The solid curve is a Gaussian fit to the distribution.

lated range of 2.74–2.85 Å reported previously.[12, 16] A weaker secondary feature is present near 3.86 Å. A similar feature was identified in both amorphous and crystalline TiO_2 and assigned to oxygen atoms bonded to the same Ti center through nearly opposite Ti–O bonds.[23] A characteristic splitting is observed in the first Ti–Ti coordination region, with maxima at 3.08 and 3.48 Å. Previous simulations and diffraction-based structural models have assigned the shorter-distance maximum predominantly to edge-sharing TiO_x polyhedra and the longer-distance maximum to corner-sharing polyhedra.[16, 23, 24] The present positions agree closely with the previously calculated ranges of 3.05–3.13 Å for edge-sharing configurations and 3.48–3.59 Å for corner-sharing configurations.[16, 23] Thus, although structural disorder substantially broadens the higher-shell features, the splitting of the Ti–Ti distribution indicates short-range order governed by the connectivity of Ti-centered polyhedra.

We have checked that the sampling structures are not

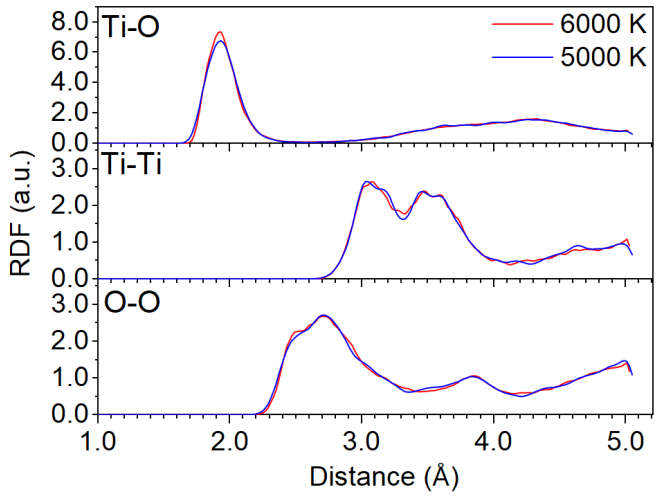


FIG. 5. Partial radial distribution functions (RDFs) for the Ti–O, Ti–Ti, and O–O pairs in a-TiO_2 generated at 6000 K (red) and 5000 K (blue). The RDF curves at each temperature were obtained by averaging over the corresponding amorphous structures, with a radial-grid width of $\Delta r = 0.02$ Å used in the calculations.

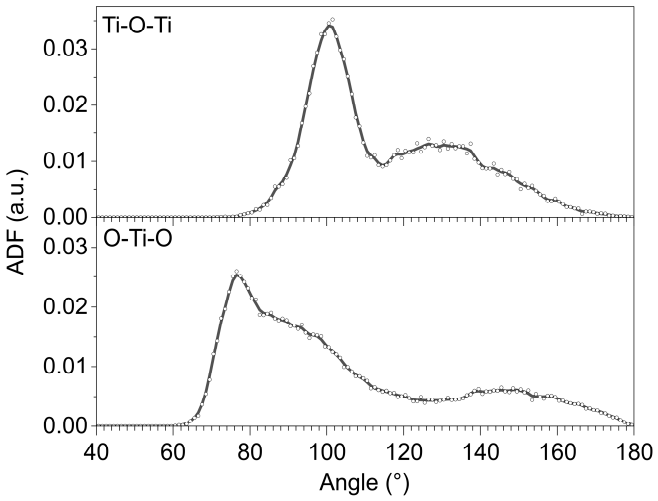


FIG. 6. Angular distribution functions (ADFs) in a-TiO_2, averaged over the 100 structures of the common-volume ensemble for Ti–O–Ti angle (top) and O–Ti–O angle (bottom). Open circles show the raw results obtained on an angular grid of $\Delta\theta = 1°$. Solid lines are for guiding the eye.

sensitive to the choice of temperature as long as a linear MSD can be achieved. To evaluate the sensitivity of the final amorphous structures to the liquid-state sampling temperature, an additional MACE-based MD simulation was performed at 5000 K. Following the same procedure as the case at 6000 K, we obtained ten new amorphous structures, based on which we obtained the RDF. As can be seen in Fig. 5, the structures are structurally similar to those obtained from MD simulations at 6000 K.

The angular distribution functions (ADFs) in Fig. 6 provide complementary information about the orientational order of these local units. The O–Ti–O distribution is dominated by a broad low-angle band centered near 77°, together with a much weaker high-angle feature near 149°. A low-angle maximum near 75° has also been reported in previous amorphous models and associated with adjacent O pairs within distorted TiO_x polyhedra.[16] Compared with the ideal octahedral angles of 90° and 180°, the broad and shifted features demonstrate substantial polyhedral distortion and the coexistence of different Ti coordination environments. The Ti–O–Ti distribution exhibits a principal maximum near 101° and a secondary feature around 127°. This bimodal profile agrees with earlier simulations reporting a first maximum near 98–100° and a broader second contribution between approximately 118° and 136°.[7, 16] The lower- and higher-angle contributions are associated predominantly with edge- and corner-sharing TiO_x units, respectively, consistent with the split Ti–Ti RDF.

The first minimum of the Ti–O RDF at 2.53 Å was subsequently used as the cutoff distance for the coordination analysis. Sixfold-coordinated Ti is the predominant species, accounting for 57.4% of all Ti atoms, followed by TiO_5 and TiO_7 units with fractions of 28.9% and 12.1%, respectively. TiO_4 and TiO_8 units occur only rarely, with fractions of 1.4% and 0.2%, respectively. Correspondingly, 66.8% of the O atoms are threefold coordinated, whereas twofold- and fourfold-coordinated O account for 21.4% and 11.8%, respectively. Accumulating statistics over the 100 structures gives average Ti–O and O–Ti coordination numbers of 5.8 and 2.9, respectively. The calculated average coordination numbers are close to the values obtained from previous studies.[16, 23] They are also consistent with diffraction-derived estimates within the reported uncertainties.[12] Nevertheless, the predominance of TiO_6 and OTi_3 environments, together with substantial populations of under- and overcoordinated species, is structural characteristic of a-TiO_2. Overall, amorphization largely preserves the local Ti–O building blocks while redistributing their coordination states, angular geometries, and connectivity.

D. Electronic structure of a-TiO_2

Figure 7(a) shows the band gaps of the 100 structures of the common-volume ensemble. They span 0.80 eV, from 2.92 to 3.72 eV, with an ensemble mean of $\bar{E}_g = 3.44$ eV and a sample standard deviation of $s = 0.12$ eV. The ensemble mean exceeds the gaps of all three crystalline polymorphs obtained with the same functional: rutile (2.92 eV), anatase (3.19 eV), and brookite (3.37 eV). The corresponding differences are 0.53, 0.25, and 0.08 eV, respectively, and 99, 97, and 76 of the 100 configurations lie above these values. The relative ordering of the rutile and anatase gaps reproduces that reported from HSE06 and G_0W_0 calculations. [21] Within the ensemble, the gaps of most configurations fluctuate about a well-defined mean, while a small mi-

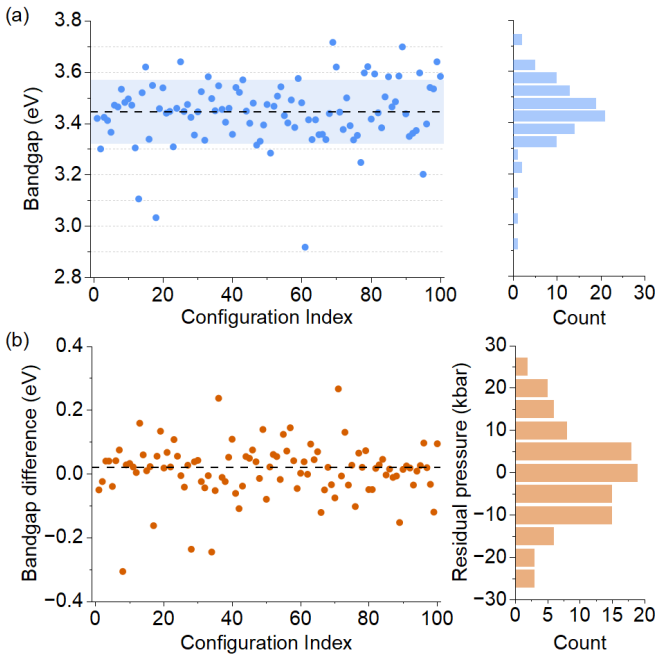


FIG. 7. Band-gap statistics and residual pressures of a-TiO_2. The band gaps were calculated at the Γ point using the HSE06 functional with an exact-exchange parameter of $\alpha = 0.18$. (a) Band gaps of the 100 common-volume structures (left) and their distribution with a bin width of 0.05 eV (right). The horizontal dashed line marks the ensemble mean of 3.44 eV, and the shaded region denotes the $\pm\sigma$ interval (3.32–3.57 eV). (b) Band-gap differences between the variable-cell-relaxed and common-volume structures (left), with the horizontal dashed line indicating the mean difference of 0.02 eV, and the distribution of residual hydrostatic pressures for the 100 common-volume structures (right).

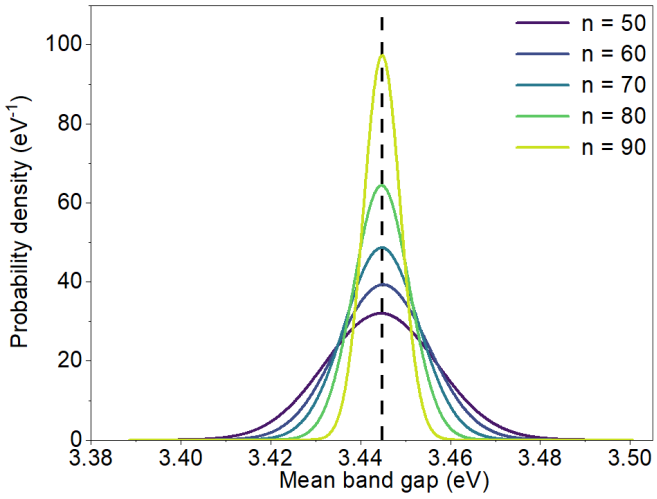


FIG. 8. Gaussian-fitted probability-density distributions of the mean band gap obtained from 10,000 random samples drawn from the 100 configurations for each subset size of $n =$ 50, 60, 70, 80, and 90. The vertical dashed line marks the full-ensemble mean of 3.44 eV.

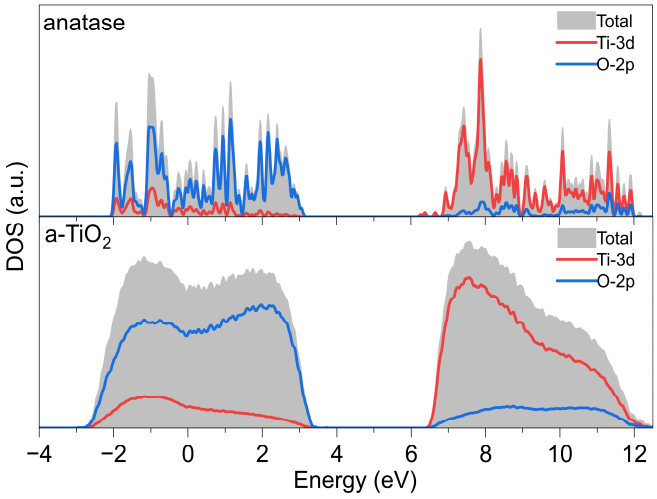


FIG. 9. Densities of states for anatase (top) and amorphous TiO_2 (bottom), calculated with the HSE06 functional using $\alpha = 0.18$. The a-TiO_2 curves are averaged over the ensemble of 100 structures. All DOS plots are aligned to the Ti 3s core-level peaks.

nority are substantially reduced. Taken together, these observations show that the gap of a-TiO_2 is not a single well-defined quantity at the computational level, but a distribution whose width is set by the structural diversity of the configurations sampled. A value obtained from any single melt–quench simulation may differ from the ensemble average by more than 0.2 eV.

Because the band-gap statistics in Fig. 7(a) were obtained from the common-volume ensemble, we further assessed the influence of this constraint. Across the 100 common-volume configurations, the residual pressures as shown in Fig. 7(b) (right) have a signed mean of -0.47 kbar. For comparison, the band gaps were also calculated using the HSE06 functional for the variable-cell-relaxed structure without setting the common volume. Fig. 7(b) (left) shows that the band gap differences between the two sets of structures. The average band gap from the variable-cell-relaxed structures is 3.46 eV, which is nearly the same as that from the common-volume structures of 3.44 eV, suggesting that as long as the sampling set of structures are sufficiently large, the residual pressure does not affect the average band gap concerned in this work. To examine the statistical convergence of the ensemble-averaged band gap, random subset sampling was performed using the 100 configurations. For each subset size of $n = 50$, 60, 70, 80, and 90, we generated 10 000 subsets. The distributions of the corresponding mean band gaps were fitted using Gaussian functions. The fitted centers remain consistent with the full-ensemble mean of 3.44 eV, whereas the full width at half maximum (FWHM) decreases monotonically from 0.029 eV at $n = 50$ to 0.010 eV at $n = 90$, as shown in Fig. 8. These results demonstrate the sufficient convergence of the ensemble mean using 100 configurations.

To identify the origin of the larger mean gap of a-

TiO_2, the ensemble-averaged desnity of states (DOS) of the 100 common-volume structures shown in Fig. 9 was aligned using the Ti 3*s* semicore level as an internal reference. The mean VBM and CBM of *a*-TiO_2 lie 0.13 and 0.36 eV above those of anatase, respectively. Both edges thus move upward, and the gap widens because the conduction edge moves further than the valence edge ($\Delta E_{\rm g} = \Delta E_{\rm CBM} - \Delta E_{\rm VBM} = 0.24$ eV). The projected DOS shows that the valence and conduction states are dominated by O 2*p* and Ti 3*d* states, respectively. In both cases the band edge moves upward while the centroid of the corresponding projected states moves slightly downward, by 0.19 eV for Ti 3*d* and 0.08 eV for O 2*p*, which produces opposite changes in the two edge-to-centroid separations. The Ti 3*d* centroid moves from 2.68 to 2.13 ± 0.07 eV above the CBM, a reduction of 21%, while the separation between the O 2*p* centroid and the VBM increases from 2.49 to 2.70 ± 0.10 eV. This conduction-band-dominated response constitutes the origin of the wider gap obtained for *a*-TiO_2.

IV. CONCLUSIONS

We conducted a computational study on the amorphous TiO_2 to gain a statistical view on its atomic and electronic structures. We employed a machine-learning interatomic potential to carry out molecular dynamics for 100,000 steps at 6000 K to extract 100 liquid configurations, which were cooled down to 0 K at a rate of $1\,{\rm K\,fs^{-1}}$. Variable-cell relaxations were then conducted on these configurations yielding a mean density of $3.94\ {\rm g\,cm^{-3}}$. As the PBEsol functional can well reproduce the experimental densities of all the three known crystal phases within $0.02\ {\rm g\,cm^{-3}}$, we hold confidence on the obtained density for the amorphous phase. The 100 configurations were then relaxed with the mean density to generate the ensemble of amorphous TiO_2. With this ensemble, we determined the coordination numbers of Ti and O. For Ti, the 5-, 6- and 7-coordinations are 28.9%, 57.4% and 12.1%, respectively. For O, the 2-, 3- and 4-coordinations are 21.4%, 66.8% and 11.8%, respectively. We further analyzed the band gaps of this ensemble of amorphous TiO_2. Using the fraction of 0.18 for the exact-exchange contribution to the hybrid HSE06 functional, the mean band gap was obtained to be 3.44 eV, which is greater than those of three crystalline phases. The large band gap was attributed to the narrowed Ti 3*d* band due to distorted atomic structures.

ACKNOWLEDGEMENTS

This work was supported by the Shanghai Explorer Project (Grant No. 24TS1403200).

[1] Marcelis E J, ten Elshof J E and Morales-Masis M 2024 *Adv. Opt. Mater.* **12** 2401423

[2] Eddy D R, Permana M D, Sakti L K, Sheha G A N, Solihudin, Hidayat S, Takei T, Kumada N and Rahayu I 2023 *Nanomaterials* **13** 704

[3] Ghamarpoor R, Fallah A and Jamshidi M 2024 *ACS Omega* **9** 25457

[4] Rafique M, Hajra S, Irshad M, Usman M, Imran M, Assiri M A and Ashraf W M 2023 *ACS Omega* **8** 25640

[5] Dong Y, Abbasi M, Meng J, German L, Carlos C, Li J, Zhang Z, Morgan D, Hwang J and Wang X 2023 *Nat. Commun.* **14** 1865

[6] Illarionov G A, Morozova S M, Chrishtop V V, Einarsrud M A and Morozov M I 2020 *Front. Chem.* **8** 724

[7] Meng J, Abbasi M, Dong Y, Carlos C, Wang X, Hwang J and Morgan D 2023 *Nanoscale* **15** 718

[8] Nunez P, Richter M H, Piercy B D, Roske C W, Cabán-Acevedo M, Losego M D, Konezny S J, Fermín D J, Hu S, Brunschwig B S and Lewis N S 2019 *J. Phys. Chem. C* **123** 20116

[9] Hu S, Shaner M R, Beardslee J A, Lichterman M F, Brunschwig B S and Lewis N S 2014 *Science* **344** 1005

[10] Kim I S, Haasch R T, Cao D H, Farha O K, Hupp J T, Kanatzidis M G and Martinson A B F 2016 *ACS Appl. Mater. Interfaces* **8** 24310

[11] Yang J, Wang Y, Li W, Wang L, Fan Y, Jiang W, Luo W, Wang Y, Kong B, Selomulya C, Liu H K, Dou S X and Zhao D 2017 *Adv. Mater.* **29** 1700523

[12] Petkov V, Holzhüter G, Tröge U, Gerber Th and Himmel B 1998 *J. Non-Cryst. Solids* **231** 17

[13] Zhang H, Chen B, Banfield J F and Waychunas G A 2008 *Phys. Rev. B* **78** 214106

[14] Mavračić J, Mocanu F C, Deringer V L, Csányi G and Elliott S R 2018 *J. Phys. Chem. Lett.* **9** 2985

[15] Kaur K and Singh C V 2012 *Energy Procedia* **29** 291

[16] Prasai B, Cai B, Underwood M K, Lewis J P and Drabold D A 2012 *J. Mater. Sci.* **47** 7515

[17] Pham H H and Wang L W 2015 *Phys. Chem. Chem. Phys.* **17** 541

[18] Landmann M, Köhler T, Köppen S, Rauls E, Frauenheim T and Schmidt W G 2012 *Phys. Rev. B* **86** 064201

[19] Köhler T, Turowski M, Ehlers H, Landmann M, Ristau D and Frauenheim T 2013 *J. Phys. D: Appl. Phys.* **46** 325302

[20] Mora-Fonz D, Kaviani M and Shluger A L 2020 *Phys. Rev. B* **102** 054205

[21] Landmann M, Rauls E and Schmidt W G 2012 *J. Phys.: Condens. Matter* **24** 195503

[22] Stojkovic M, Linscott E and Marzari N 2026 *Phys. Rev. Mater.* **10** 025403

[23] Calegari Andrade M F and Selloni A 2020 *Phys. Rev. Mater.* **4** 113803

[24] Ding Z and Selloni A 2023 *J. Chem. Phys.* **159** 024706

[25] Kang Y, Liu Z P and Li Y F 2026 *J. Am. Chem. Soc.* **148** 23088

[26] Sivaraman G, Csányi G, Vazquez-Mayagoitia A, Foster I T, Wilke S K, Weber R and Benmore C J 2022 *J. Phys.*

Soc. Jpn. **91** 091009
[27] Batatia I, Kovács D P, Simm G N C, Ortner C and Csányi G 2022 *Advances in Neural Information Processing Systems* **35** 11423
[28] https://cloud.hzwtech.com/, DS-PAW package integrated in Device Studio from Hongzhiwei Technology, China, accessed August 1, 2026.
[29] Kresse G and Joubert D 1999 *Phys. Rev. B* **59** 1758
[30] Blöchl P E 1994 *Phys. Rev. B* **50** 17953
[31] Perdew J P, Ruzsinszky A, Csonka G I, Vydrov O A, Scuseria G E, Constantin L A, Zhou X and Burke K 2008 *Phys. Rev. Lett.* **100** 136406
[32] Nosé S 1984 *J. Chem. Phys.* **81** 511
[33] Hoover W G 1985 *Phys. Rev. A* **31** 1695
[34] Chai J, Ming C, Zeng Y, Liu Z and Sun Y Y 2025 *Phys. Rev. B* **111** 035433
[35] Larsen A H, Mortensen J J, Blomqvist J, *et al.* 2017 *J. Phys.: Condens. Matter* **29** 273002
[36] Heyd J, Scuseria G E and Ernzerhof M 2003 *J. Chem. Phys.* **118** 8207
[37] Krukau A V, Vydrov O A, Izmaylov A F and Scuseria G E 2006 *J. Chem. Phys.* **125** 224106
[38] Howard C J, Sabine T M and Dickson F 1991 *Acta Crystallogr. B* **47** 462
[39] Meagher E P and Lager G A 1979 *Can. Mineral.* **17** 77
[40] Deskins N A, Du J and Rao P 2017 *Phys. Chem. Chem. Phys.* **19** 18671